Supporting Information: Modeling The Navigating Forces Behind BSA Aggregation in a Microfluidic Chip

Zahra Haghparas,[a] Mohammadjavad Bouloorchi Tabalvandani,[b] Payam Arghavani,[a] Soroush Behjati Hosseini,[a] Majid Badieirostami,*[b] Mehran Habibi-Rezaei[c] and Ali Akbar Moosavi-Movahedi*[a]

[a]*Institute of Biochemistry and Biophysics, University of Tehran, Tehran, Iran*

[b]*MEMS Lab, School of Electrical and Computer Engineering, College of Engineering, University of Tehran, Tehran, Iran*

[c]*School of Biology, College of Science, University of Tehran, Tehran, Iran*

Corresponding Authors: mbadiei@ut.ac.ir (M. Badieirostami) and moosavi@ut.ac.ir (A. A. Moosavi-Movahedi)

Designed microfluidic chip

According to research on protein aggregation in microfluidic chips,[1–3] a chip was designed and fabricated with a serpentine channel containing seven loops to promote complete protein aggregation. The fabricated microfluidic chip is shown in Fig. S1. The chip incorporated two inlets for protein introduction to investigate the influence of advective mixing on this process. Two separate chips were constructed (Fig. S2) with distinct outlet reservoir locations: M_1, located after three loops (Fig. S2A), and M_2, positioned at the channel's end (Fig. S2B), allowing the formation of the aggregates to be monitored.

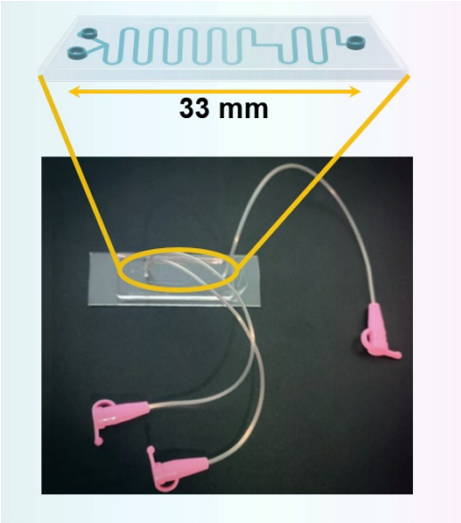

Fig. S1 Fabricated microfluidic chip.

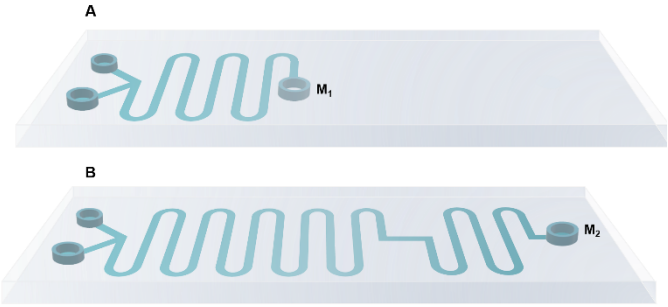

Fig. S2 scheme of microfluidic chips with (A) M_1 and (B) M_2 reservoirs.

Purpose-built heating plate

A custom heating plate facilitated precise temperature control for the microfluidic chip. The hotplate utilized a heating element, thermocouple, and digital thermostat. The 5-meter heating element, powered by standard 220V electricity without a voltage converter, achieved temperatures

up to 400 °C. The thermocouple and thermostat ensured accurate temperature setting and monitoring. The heating element was spirally adhered between two 20 cm square Pyrex glasses using thermal adhesive. This design allowed a central cavity to accommodate the chip and enabled real-time microscopic imaging within the microchannels while maintaining the desired temperature. A schematic of the heating plate is visible in Fig. S3.

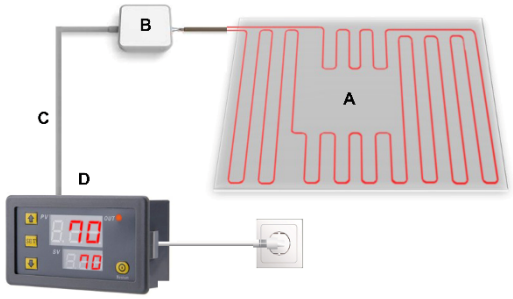

Fig. S3 The purpose-built hotplate contains (A) a glass hotplate, (B) an adaptor, (C) a thermocouple, and (D) a digital thermostat.

Microscopic visualization of BSA aggregation in vial

Microscopic visualization revealed the progression of protein aggregation within the vial over time (Fig. S4). Figs. S4A and S4B show images taken 5 and 10 minutes after exposure to 70 °C, respectively. No ThT fluorescence (left panels) is observed, indicating minimal aggregation at this stage. However, the corresponding SEM images (right panels) reveal the formation of early-stage clusters. Fig. S4C depicts the structures formed after 30 minutes. A slight increase in ThT emission suggests some aggregation, while the SEM image confirms the presence of larger clusters. Finally, Fig. S4D showcases the dramatic change after 6 hours. The left panel displays a significant ThT signal, indicating extensive amyloid-like aggregates formation. The corresponding SEM image visualizes these mature aggregates.

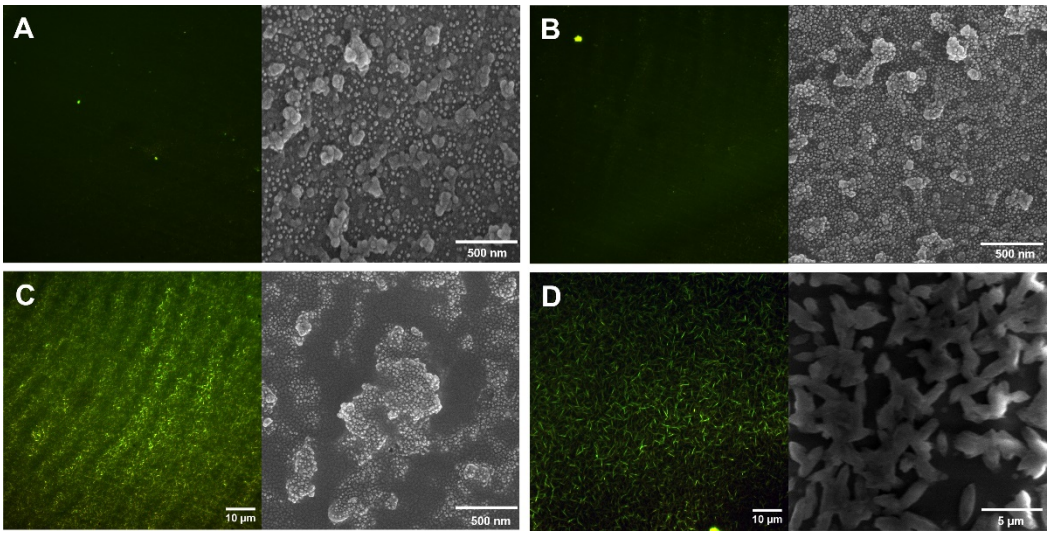

Fig. S4 Microscopic visualization of BSA aggregation pathway at 2.5 mg.ml^{-1} following exposure to 70 °C. (A) 5 minutes, (B) 10 minutes, (C) 30 minutes, (D) 360 minutes. The left panels show fluorescence microscopy with 5 mM ThT staining and the right panels show SEM images.

Cell viability assay

The cytotoxicity of the formed amyloid-like aggregates was assessed using the MTT assay on MCF-7 breast cancer cells (Fig. S5).

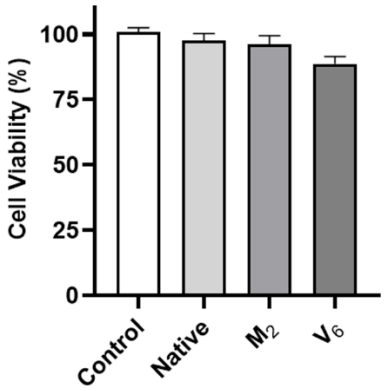

Fig. S5 MCF-7 cell viability after incubation with BSA samples. Cells were treated with 30 µg.ml^{-1} of native BSA, V_6, and M_2 samples, and viability was measured using the MTT assay. Data represent mean ± SEM from m independent repetitions (m=3).

Modeling the behavior of BSA clusters in the microfluidic chip

An ensemble of 200 particles was uniformly distributed throughout the serpentine microchannels at t = 0 to visualize the behavior of BSA clusters inside the channel. The simulation results demonstrated the gradual deposition of the clusters onto the sidewalls as time passed (Movie S1). In this movie, the cold spectrum (blue) refers to slower particles, and the hot spectrum (red)

indicates faster clusters. The simulation considered three key factors: Stokes' drag force, Brownian movement, and particle-particle interactions. The simulated Brownian movement is defined as equation 1,

$$F_B = \zeta \sqrt{\frac{12\pi k_B \mu T r_p}{\Delta t}} \quad (1)$$

where ξ is a random number with the normal distribution (zero mean and standard deviation of one), k_B signifies Boltzmann constant, μ stands for the dynamic viscosity of the fluid, T illustrates the temperature of the fluid in Kelvin, r_p represents the particle radius, and Δt is the time step taken by the solver. The Stokes' drag force is denoted as equation 2,

$$F_D = \left(\frac{1}{\tau_p}\right) m_p (u - v) \quad (2)$$

where m_p is the particle mass, τ_p represents the particle velocity response time, **u** symbolizes the fluid velocity, and **v** corresponds to the particle velocity. Equation 3 determines the particle velocity response time for Stokes' drag law,

$$\tau_p = \frac{\rho_p d_p^2}{18\mu} \quad (3)$$

where ρ_p, d_p^2, and μ denote particle density, diameter, and the fluid's dynamic viscosity, respectively. This combined approach allowed us to investigate how the interplay of these forces influenced the movement and deposition of BSA clusters within the microfluidic system. As shown in Movie S1, faster particles move swiftly through the channel, while slower particles deposit onto the channel sidewalls leading to conformational changes in the deposited particles. In Movie S1, a segment of the microchannel is captured at different time points, as illustrated in Fig. S6. The dynamic movement of spherical particles (300 nm in diameter) over time indicates that slower particles (cold spectrum) tend to deposit onto the channel sidewalls.

Movie S1 The BSA cluster's behavior in the microfluidic chip is shown here for 300 nm particles in diameter, which is downloadable using the below link. The cold-spectrum refers to slower particles, and the hot-spectrum refers to faster clusters.

Download Movie S1: https://drive.google.com/file/d/1r2wpbTvCtuHLc3SOWV-IgTWzwoIFqVIM/view?usp=sharing

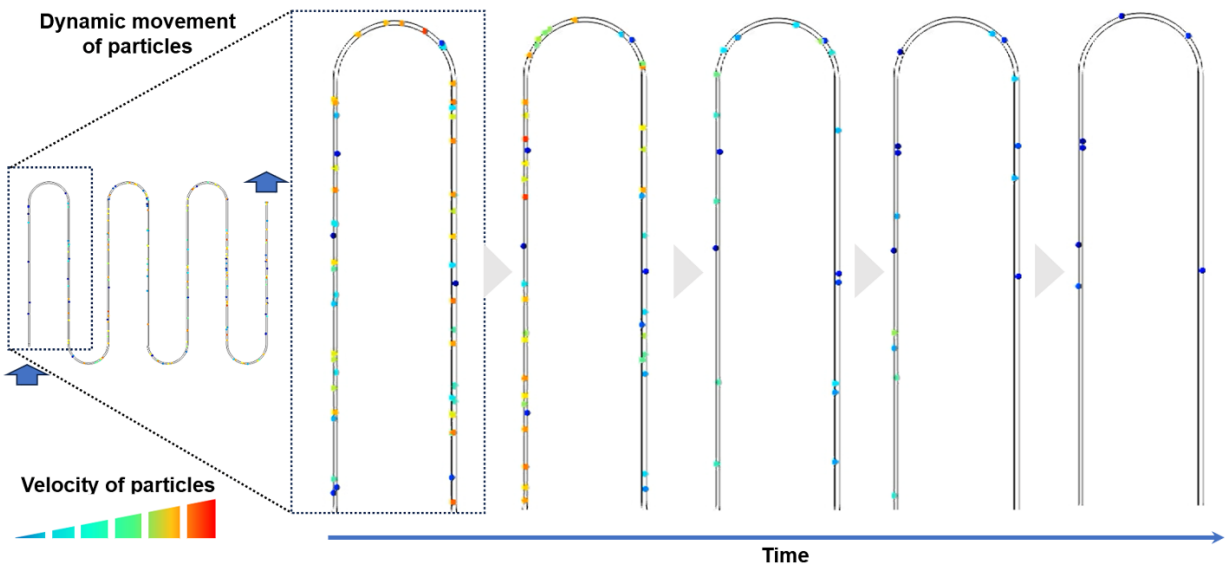

Fig. S6 Dynamic movement of 300 nm spherical particles within a microchannel segment over time. Slower particles (cold spectrum) are observed depositing onto the channel sidewalls, as captured in different time points shown in Movie S1.

This simulation was performed for particles smaller than 100 nm in diameter (50 nm to be considered). As can be seen in Movie S2, the slower particles (blue) indicated the least tendency to deposit onto the channel sidewalls.

Movie S2 The behavior of BSA clusters within the microfluidic chip is demonstrated here for 50 nm diameter particles. The data can be downloaded using the link below. The cold spectrum represents slower particles, while the hot spectrum corresponds to faster clusters.

Download Movie S2: https://drive.google.com/file/d/1svdQ0rsMfe7Jyzj9RNCgjEZwgApNq_Qn/view?usp=sharing

Heat transfer simulation in microfluidic chip

COMSOL Multiphysics simulations ensured sufficient energy transfer within the microfluidic chip to drive protein aggregation. We modeled heat transfer in the fluid under steady-state conditions to analyze heat exchange within the device. Both the channel and incoming fluid were initially set to 25 °C. The bottom boundary, representing a heated hotplate, was assigned a constant temperature of 70 °C. Other boundaries were considered thermally isolated, neglecting heat loss to the environment due to PDMS's low thermal conductivity. This simplification is justified for

this material. The heat transfer inside the fluid flowing through the channel was then solved using equations 4 and 5 as described below,

$$\rho C_p u.\nabla T + \nabla.q = Q + Q_{vd} \quad (4)$$

$$q = -k\nabla T \quad (5)$$

where ρ is the fluid density, C_p is the specific heat capacity, q is the heat flux by conduction, Q_{vd} is the viscous dissipation in the fluid, Q represents heat sources other than viscous dissipation, k is the thermal conductivity, and ∇T is the temperature gradient across the boundary. As shown in Fig. S7, the temperature profile within the initial section of the channel indicates a rapid rise in the fluid temperature to the desired 70 °C. This temperature is maintained throughout the channel, confirming sufficient energy delivery for the aggregation process.

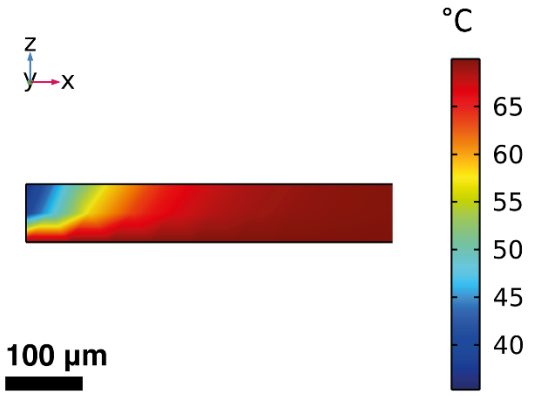

Fig. S7 Simulated temperature profile within the microfluidic channel.

Gibbs free energy

Equation 6 was employed to calculate the Gibbs free energy difference (ΔG) for BSA thermal denaturation (aggregation in bulk) within a two-state model (N and U).[4]

$$\Delta_N^U G = \Delta_N^U H(T) - T\Delta_N^U S(T) \quad (6)$$

The enthalpy and entropy were identified by equations 7 and 8, respectively.[4]

$$\Delta H(T) = \Delta H(T_e) + \int_{T_e}^{T} \Delta_N^U C_p \, dT \quad (7)$$

$$\Delta S(T) = \frac{\Delta H(T_e)}{T_e} + \int_{T_e}^{T} \Delta_N^U C_p \, d\ln T \qquad (8)$$

Here, T_e represented the temperature at which both states had an equal probability. Assuming $\Delta_N^U C_p$ to be independent of temperature, driven by the following equation,[4]

$$\Delta_N^U G(T) = \Delta_N^U H(T_e)\left(1 - \frac{T}{T_e}\right) - \Delta_N^U C_p(T_e)\left(T_e - T + T\ln\frac{T}{T_e}\right) \qquad (9)$$

As proven by *Ling Fu et al.*,[4] the enthalpy change for BSA aggregation at the obtained T_e (110 °C) is 44 kJ.mol^{-1}, with a corresponding ΔC_p of 0.32 kJ.K^{-1}.mol^{-1}. Using these values and Eq. 9, BSA's estimated ΔG at 70 °C is 3.9 kJ.mol^{-1}.

Thermal unfolding energy in the microfluidic chip

The required thermal unfolding energy per microchannel volume was estimated. We considered the BSA concentration (2.5 mg.ml^{-1}), its molecular weight (66,500 g.mol^{-1}), the calculated Gibbs free energy for unfolding (3.9 kJ.mol^{-1}), and an assumed microchannel volume (50 µm in width and 60 µm in height, resulting in a volume of 1.5×10^{-10} L). This analysis indicated an energy requirement of approximately 2.2×10^{-14} J per microchannel volume to activate BSA molecules.

Lennard-Jones parameters versus various particle diameters

The DLVO pair potential was visualized using MATLAB for clusters with various diameters (Fig. S8). The Lennard-Jones parameters were extracted from these visualizations, revealing a strong correlation between particle diameter and interaction strength (Table S1). Accordingly, particles smaller than 100 nm in diameter predominantly experience electrostatic repulsion. In contrast, larger particles are more prone to van der Waals attraction, leading to mutual adsorption. As shown in Table S1 the interaction strength increases with particle size.

Table S1. The Lennard-Jones potential for clusters with different diameters.

Clusters Diameter (nm)	50 nm	75 nm	100 nm	200 nm	300 nm
Intermolecular Distance (nm)	61.75	85.3	109	207.24	306

Interaction Strength (J)	-0.0994×10^{-21}	-0.322×10^{-21}	-0.62×10^{-21}	-2.46×10^{-21}	-5.02×10^{-21}

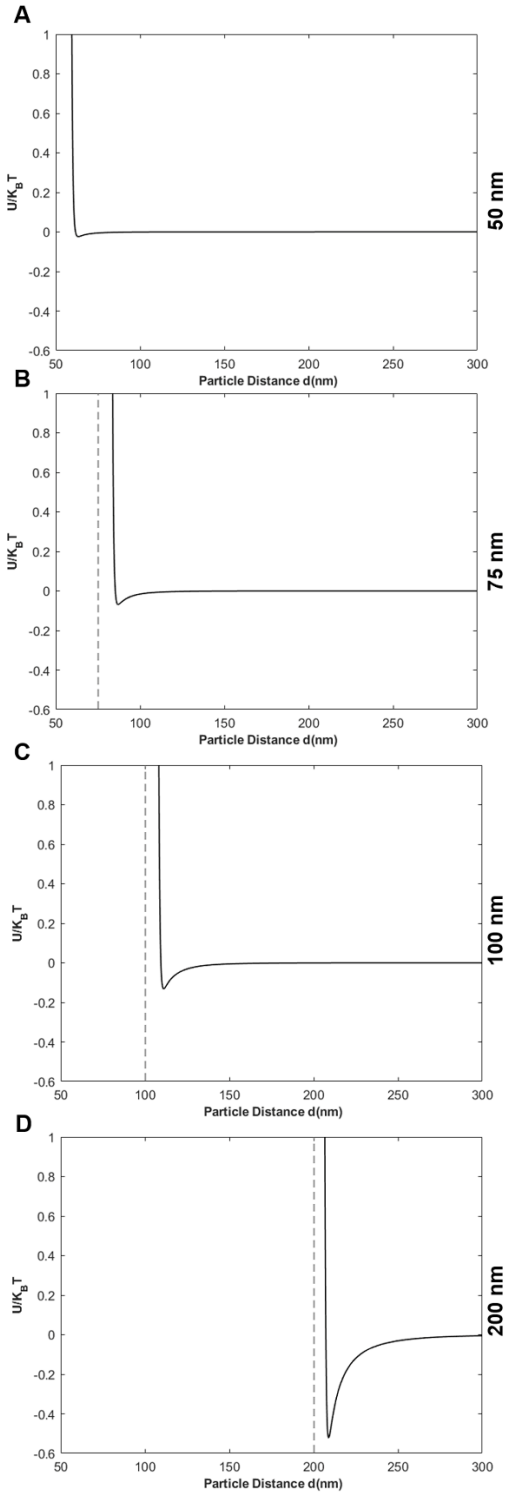

Fig. S8 Modeling the DLVO pair potential for spherical particles in a system containing 261.39 mol.m^{-3} ion at 70 °C with κ^{-1} = 0.645 nm and A = 1 k_BT. The simulations are shown for varying particle radii (r) and surface potentials (Ψ). (A) r = 25 nm, Ψ = 0.00036 mV; (B) r = 37.5 nm, Ψ = 0.00016 mV; (C) r = 50 nm, Ψ = 0.0000916 mV, and (D) r = 100 nm, Ψ = 0.000023 mV.

Raynolds number

The relative Raynolds number for particles in the microfluidic chip is calculated using equation 10,

$$Re = \frac{\rho U D_H}{\mu} \qquad (10)$$

where ρ represents the density, U (~0.01 m.s^{-1}) denotes the average velocity, D_H refers to the hydraulic diameter, and μ is the dynamic viscosity. The hydraulic diameter for a rectangular cross-section is obtained according to equation 11,

$$D_H = \frac{2 \times a \times b}{a + b} \qquad (11)$$

where a (a=50 μm) denotes the width and b (b=60 μm) refers to the height. Using equations 10 and 11, the Raynolds number is estimated at 0.6.

Ionic concentration

To prepare the solution for examinations, native BSA was dissolved in 100 mM phosphate buffer (pH 7.4). The Henderson-Hasselbalch Equation[5] (equation 12) with a fixed pKa 7.2 was used to estimate the solution's ionic concentration.

$$pH = pKa + \log\frac{[A^-]}{[HA]} \qquad (12)$$

This calculation resulted in estimated concentrations of 38.61 mM [$H_2PO_4^-$], 61.39 mM [HPO_4^{2-}], and 161.39 mM [Na^+], leading to a total ionic concentration of 261.39 mM.

Surface hydrophobicity of vials and PDMS

The contact angles of water and BSA droplets on both vial and PDMS surfaces were measured (Fig. S9). Water contact angles were significantly higher for PDMS (60 ± 1°) compared to the vial (17 ± 2°), indicating a more hydrophobic PDMS surface (Figs. S9A & S9B). Similarly, BSA droplets exhibited a higher contact angle on PDMS (89 ± 0.5°) compared to the vial (61.5 ± 1°),

suggesting preferential interaction with the hydrophobic PDMS (Figs. S9C & S9D). Notably, both the inner and outer vial surfaces are composed of polypropylene.

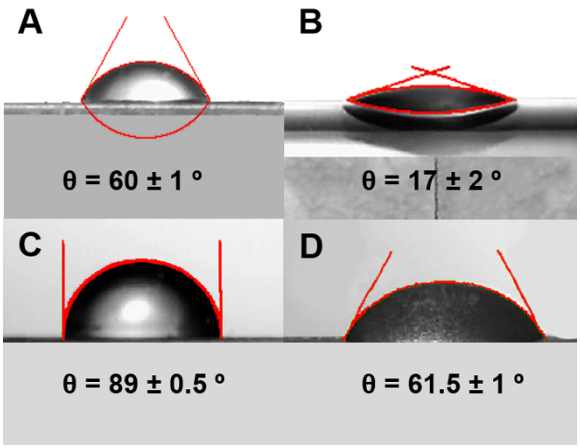

Fig. S9 Contact angle measurements. Water contact angles on (A) PDMS and (B) vial surfaces. BSA droplet contact angles on (C) PDMS and (D) vial surfaces. Data represent mean ± SEM (m=3).

Kinetics of BSA aggregation using ANS assay

The kinetics of BSA aggregation in the vial were monitored using ANS fluorescence intensity. A solution of 2.5 mg.ml^{-1} BSA in 100 mM phosphate buffer (pH 7.4) was heated at 70 °C for varying intervals (0, 5, 10, 15, 30, 45, 60, 120, 240, 360, and 780 minutes). The samples were then stained with 280 µM ANS. The fluorescence intensity at 490 nm (excited at 350 nm) was recorded over time and is visible in Fig. S10.

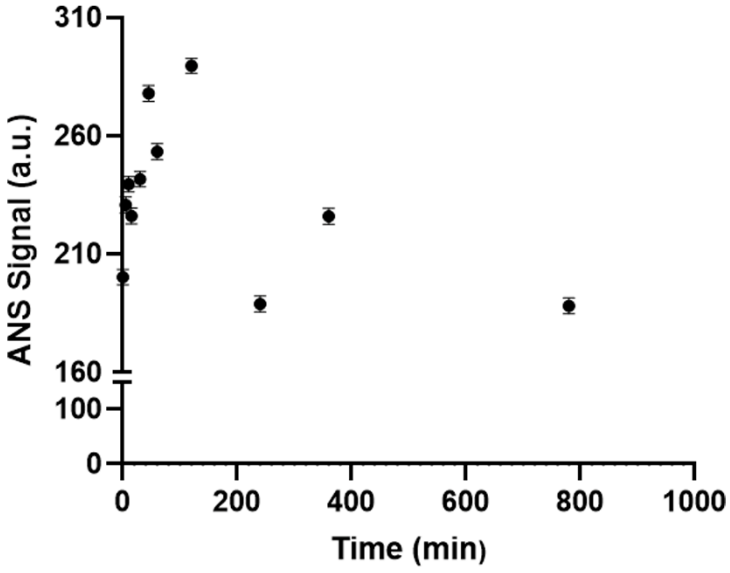

Fig. S10 Kinetics of BSA aggregation monitored by ANS fluorescence.

References

1. K.L. Saar, E.V. Yates, T. Müller, S. Saunier, C.M. Dobson and T.P.J. Knowles, *Biophys. J*., 2016, **110**, 555–560.

2. X. Weng, W. Zhao, S. Neethirajan and T. Duffield, *J. Nanobiotechnol*., 2015, **13**, 1-8.

3. F. Kashanian, M.M. Masoudi, A. Shamloo, M. Habibi-Rezaei and A.A. Moosavi-Movahedi, *Bioproc. Biosyst. Eng*., 2018, **41**, 707–714.

4. L. Fu, S. Villette, S. Petoud, F. Fernandez-Alonso and M.L. Saboungi, *J. Phys. Chem. B*., 2011, **115**, 1881–1888.

5. H.N. Po and N.M. Senozan, *J. Chem. Educ*, 2001, **78**, 1499–1503.